

Torsion as an Emergent Dark Sector: Global Consistency and Falsifiable Predictions

Alejandro Rey

Independent Researcher

<https://orcid.org/0009-0007-5052-3917>

January 2026

Abstract

We present a cosmological implementation of environmental spacetime torsion within an Einstein–Cartan framework in which the dark sector emerges as a geometric response to virialized matter. Torsion is activated only in dense environments and induces an effective late-time residual that reproduces dark-energy–like behavior while remaining dormant across the standard early-Universe observational window (BBN, recombination, and BAO calibration), thereby preserving the sound horizon and standard rulers by construction. The central falsifiable prediction is a late-time, environment-dependent modification of the inferred expansion rate, yielding testable spatial gradients in the locally inferred Hubble constant H_0 without altering early-time calibration. We implement the resulting fixed environmental backbone in a modified CLASS pipeline and confront it with late-time expansion probes, while treating BAO strictly as a fixed-backbone consistency filter (no parameter re-optimization) that delimits the viable regime rather than tuning the model. Using identical real cluster observables (f_b vs. z), datasets, and fitting protocols, particle–DM–motivated phenomenological baselines exhibit poor generalization in blind tests, whereas the environmental torsion template retains predictive performance. These results support an environment-dependent geometric origin for the dark-sector phenomenology tested here and motivate the Rey–TIDE framework.

1 Introduction

This work advances the Rey–TIDE framework, in which the dark-sector phenomenology arises as an emergent, environment-dependent geometric response of spacetime. The empirical motivation is provided by persistent anomalies associated with virialized structures. Most notably, the baryon deficit in galaxy clusters relative to the cosmic baryon fraction is accompanied by the late-time expansion anomalies targeted here. Within this framework, the phenomenology commonly attributed to dark matter and dark energy is generated by a single underlying geometric mechanism, allowing cluster-scale inconsistencies and late-time acceleration to be addressed within a unified geometric description without modifying early-Universe calibration.

The framework is formulated within the Einstein–Cartan–Sciama–Kibble (ECSK) completion of General Relativity, where torsion appears as an algebraic (non-propagating)

degree of freedom sourced by matter spin density. In the standard cosmological regime, torsion remains effectively dormant across the observable early-Universe window relevant to Big Bang Nucleosynthesis and recombination. Once nonlinear structure formation sets in, coarse-grained effective spin densities in virialized environments generate a small geometric residual contribution to the late-time background expansion, while preserving standard recombination physics and the baryon-drag sound horizon scale. Although the resulting phenomenology manifests observationally at late cosmic times, this reflects the onset of structure formation rather than a fundamental time dependence of the torsional degrees of freedom.

A critical methodological requirement for this framework is predictive generalization rather than dataset-by-dataset tuning. The analysis is therefore conducted under deliberately stringent conditions: a single fixed environmental backbone is stress-tested across multiple observables, and mismatches are interpreted as regime constraints rather than opportunities for tuning. In this context, Baryon Acoustic Oscillations (BAO) are treated strictly as a fixed-backbone consistency filter. The drag-epoch sound horizon r_d remains unchanged in the modified implementation, and the recombination sound horizon r_s is likewise preserved, such that BAO delimits viable environmental backbones while remaining external to parameter inference.

This paper constitutes the third step of the Rey-TIDE program. Paper I established observational evidence for environmentally activated torsion signatures in virialized systems, including galaxy clusters and gravitational lensing [18]. Paper II mapped the resulting environmental backbone while preserving early-Universe calibration [19]. Here (Paper III) we implement the resulting fixed backbone in a Boltzmann solver and confront it with late-time expansion probes under the methodological constraints described above, including a blind holdout validation (70% training / 30% holdout) designed to separate genuine predictive power from phenomenological overfitting.

The analysis culminates in a sharp, falsifiable signature that follows directly from environmental activation: the locally inferred Hubble constant should exhibit a measurable dependence on the surrounding large-scale environment, with specific cross-correlations to structure tracers. This prediction provides a direct observational test of the framework and can be confirmed or ruled out by upcoming surveys (Sec. 6).

2 Environmental activation and coarse-graining

In ECSK gravity, torsion is algebraic (non-propagating) and sourced only by local matter spin density; it vanishes identically in its absence.

We parametrize torsion activation in coarse-grained environments via:

$$A(\rho_{\text{env}}) \equiv \frac{(\rho_{\text{env}}/\rho_{\text{env},*})^n}{1 + (\rho_{\text{env}}/\rho_{\text{env},*})^n}, \quad (1)$$

where $\rho_{\text{env}} \equiv 3M_\Delta/(4\pi R_\Delta^3)$ (with $\Delta = 200$), inferred from X-ray, SZ, or weak-lensing mass estimates of virialized structures (Paper I). The parameters $\rho_{\text{env},*}$ and n are fixed environmental thresholds from structure formation, not free cosmological functions. Here $\rho_{\text{env},*}$ denotes the environmental activation threshold and should not be confused with the cosmological critical density. This form emerges naturally from averaging the Cartan equation over spin-carrying matter distributions, with $\rho_{\text{env},*}$ marking the virialization threshold. Unlike chameleon-type screening, no additional fields are introduced; this

represents purely algebraic elimination of torsion after coarse-graining. Limits: In low-density regimes ($\rho_{\text{env}} \ll \rho_{\text{env},*}$), $A \rightarrow 0$ and GR is recovered. In virialized environments ($\rho_{\text{env}} \gg \rho_{\text{env},*}$), $A \rightarrow 1$ and torsion effects become relevant. The homogeneous average of local corrections contributes to the effective term Λ_{eff} below.

3 Emergent Geometric Residual and Effective Cosmological Contribution

Upon algebraic elimination of torsion in ECSK gravity, local spin–spin interactions generate quadratic contributions to the effective energy–momentum tensor. When averaged over virialized structures, these terms induce a homogeneous residual contribution to the background geometry. We therefore define an effective cosmological contribution not as a fundamental constant nor as a time-dependent degree of freedom, but as an environmentally sourced geometric residual:

$$\Lambda_{\text{eff}}[z] = \frac{3\kappa^2}{8} \int_{M_{\min}}^{M_{\max}} A(\rho_{\text{env}}(M)) T_0^2 \left(\frac{M}{M_{\text{crit}}} \right)^{2\alpha} n(M, z) \frac{dM}{M}, \quad (2)$$

where $\kappa = 8\pi G$, $A(\rho_{\text{env}})$ is the activation function from Eq. (1), $T_0 = 0.62$ (dimensionless coupling strength calibrated from Paper II cluster analysis), $\alpha = 0.35$ (mass-scaling exponent), $M_{\text{crit}} = 10^{14} M_{\odot}$ (critical mass threshold), and $n(M, z)$ is the Tinker et al. (2008) halo mass function. Integration limits are $M_{\min} = 10^{12} M_{\odot}$ and $M_{\max} = 10^{16} M_{\odot}$, covering the cluster-dominated regime. The redshift dependence enters solely through $n(M, z)$; no explicit time evolution is introduced in the torsion sector. This formulation makes explicit that Λ_{eff} is not a fundamental constant but an environmentally sourced geometric residual. The numerical evaluation at $z \lesssim 1$ yields $\Lambda_{\text{eff}} \approx 1.2 \times 10^{-52} \text{ m}^{-2}$, corresponding to $\Omega_r \approx 0.15$ for $H_0 = 74.08 \text{ km s}^{-1} \text{ Mpc}^{-1}$. In this sense, Λ_{eff} should be interpreted as a macroscopic descriptor rather than a fundamental constant. Much like temperature in statistical mechanics, it does not correspond to a microscopic degree of freedom but to the coarse–grained response of spacetime geometry to the distribution of bound, spin–carrying matter. Individual spin–torsion interactions remain locally algebraic and non–propagating, yet their environmental averaging produces a small but coherent geometric residual at late times. As a consequence,

$$\Lambda_{\text{eff}}[\rho_{\text{env}}] \rightarrow 0 \quad \text{in the early Universe,} \quad (3)$$

when virialized structures are absent. This preserves the standard physics of recombination, the sound horizon r_s , and all early-time cosmological observables.

4 Cosmological Implementation

CLASS v3.3.4 is modified to include environmental density $\rho_{\text{env}}(z)$ as input. The background equation incorporates Λ_{eff} , verified numerically in the modified CLASS runs to preserve the sound horizon scales r_s and r_d to machine precision. Full implementation details are reported in Paper II; here we focus on observational constraints. **BAO consistency check:** We impose BAO as a distance-ratio check on the fixed backbone. BAO observables use the sound horizon at the baryon-drag epoch, r_d , as the standard ruler. In our implementation, the drag scale is held fixed at $r_d = 147.09 \text{ Mpc}$ (Planck 2018), verified

in CLASS to machine precision. Early-time physics is preserved: both the recombination sound horizon r_s and the drag scale r_d remain unchanged by construction. BAO is not a fit parameter; it bounds the viable environmental backbone regimes.

4.1 Mathematical Framework for Global Constraints

To ensure transparency, we explicitly define the effective expansion rate $H(z)$. This is the rate used throughout the late-time tests. In the late-time regime ($z \lesssim 2$), we parameterize the background as an effective flat expansion history. Spatial flatness is assumed in the effective background, as the early-Universe physics that fixes the global geometry is left unmodified. Late-time environmental torsion therefore does not alter the large-scale spatial curvature.

$$H(z) = H_0 \sqrt{\Omega_{m,\text{eff}}(1+z)^3 + (1-\Omega_{m,\text{eff}})}, \quad (4)$$

where $\Omega_{m,\text{eff}}$ represents the total effective matter density governing the background evolution. This is consistent with the form used in Appendix A. In the Rey-TIDE framework, this quantity is decomposed as

$$\Omega_{m,\text{eff}} = \Omega_b + \Omega_\tau, \quad (5)$$

where Ω_τ encodes the effective geometric torsion response emerging within virialized environments (see Section 2 and Appendix A). For the fixed environmental backbone inherited from Paper II, we adopt

$$\Omega_{m,\text{eff}} = 0.20, \quad (6)$$

which encompasses $\Omega_b \simeq 0.05$ and $\Omega_\tau \simeq 0.15$.

Environmental Backbone Transfer: Paper II → Paper III

The connection between the cluster-scale baryon-fraction analysis (Paper II) and the background cosmology (Paper III) is established through the environmental coupling parameter ξ_{env} . The following table summarizes the quantitative mapping: The quantitative mapping from ξ_{eff} to Ω_τ follows from the environmental coarse-graining integral specified in Eq. (2). The cluster-calibrated torsion amplitude $T(M)$ is integrated over the halo mass function $n(M, z)$ following the Tinker et al. (2008) formalism. For the Paper II best-fit cluster parameters ($\xi_{\text{eff}} = 0.4901$, $C_{\text{cl}} = 0.1541$), this mass-weighted integration yields $\Omega_\tau \approx 0.15$ as adopted throughout this work. The age of the Universe t_0 is then computed through the standard cosmological integral:

$$t_0 = \int_0^\infty \frac{dz}{(1+z)H(z)}. \quad (7)$$

By adopting the lower effective matter density $\Omega_{m,\text{eff}} = 0.20$ compared to the Λ CDM baseline ($\Omega_m \simeq 0.31$), the integral yields a longer cosmic expansion duration, effectively decoupling the high local H_0 value from the so-called “young Universe” problem. From a physical standpoint, this formulation preserves early-time consistency: torsion remains algebraically inactive in low-density regimes, ensuring that recombination physics, baryon drag, and the sound horizon r_s remain strictly Einsteinian. The late-time activation of Ω_τ thus provides a purely geometric adjustment to the expansion history without invoking new dynamical fields or exotic fluids.

Table 1: Environmental Backbone Transfer: Paper II (Cluster Analysis) → Paper III (Cosmological Background)

Paper II: Galaxy Cluster Analysis (N=200 blind test)	Best-fit Value	Derivation
Baryon fraction model: $f_b(z) = \frac{C_{\text{cl}}}{1+\xi\sqrt{z}}$	$C_{\text{cl}} = 0.1541, \xi = 0.4901$	Blind cross-validation
Normalization C_{cl}	0.1541	Fitted to 200 clusters
Torsion coupling ξ_{eff}	0.4901	Cluster scale
Virial amplification $e_{\Delta\tau}$	5.9 ± 0.8	Transport equation
Paper III: Cosmological Background Mapping		
Halo mass integral: $\int_0^\infty T^2(M) n(M, z) M dM$	Mass-weighted torsion	Coarse-grained residual
Coarse-grained residual Λ_{eff}	$8\pi G \times 0.15\rho_{\text{crit},0}$ (effective normalization)	HMF integration
Torsion density Ω_τ	0.15	Derived from Paper II
Baryonic component Ω_b	0.0493	Planck 2018
Effective total $\Omega_{m,\text{eff}}$	0.20	Fixed backbone

5 Results

Results stress-test the fixed environmental backbone against late-time probes without re-optimization. BAO is evaluated via a reduced distance-ratio check and the full likelihood, while SN+CC consistency is treated as a necessary condition and BAO discrepancies serve as regime constraints. We also report a blind cross-validation on the Paper II cluster dataset for Rey-TIDE and alternative templates under an identical protocol.

5.1 Late-time background consistency and the Age of the Universe

The backbone parameters ($H_0 \approx 74.08$, $\Omega_{m,\text{eff}} \approx 0.20$) are first confronted with the combined dataset of Pantheon+ Type Ia Supernovae (SN). Cosmic Chronometers (32 points; Moresco et al. 2022 compilation) are included as an independent late-time expansion probe. Fig. 4 shows that the fixed backbone provides a consistent description of both direct $H(z)$ measurements (CC; left panel) and the SN Hubble diagram (right panel) over the late-time range. Crucially, the statistical performance of the fixed backbone is robust. As shown in the residual analysis (Fig. 3), the pull distribution is approximately Gaussian, centered near zero, with dispersion consistent with unity, indicating that the environmental framework provides an unbiased description of the distance ladder without requiring additional nuisance parameters.

The Age Anomaly Resolution: Perhaps the most significant consequence of the Rey-TIDE backbone is the inferred age of the Universe. Standard Λ CDM fits forcing $H_0 \approx 74$ km s⁻¹ Mpc⁻¹ typically yield a dangerously young universe ($t_0 \approx 12.8$ Gyr), in tension with the ages of the oldest globular clusters. In contrast, due to the lower effective matter

density $\Omega_{m,\text{eff}} = 0.20$ required by the torsional framework, the cosmic time integral yields:

$$t_0^{\text{RT}} \approx 14.20 \text{ Gyr.} \quad (8)$$

This result naturally accommodates the oldest stellar populations while simultaneously resolving the H_0 tension, a feat that standard high- H_0 solutions fail to achieve.

5.2 Resolution of the S_8 Tension: The $P(k)$ Suppression

Beyond the expansion history, the Rey–TIDE framework makes specific predictions regarding the growth of structure. Unlike ΛCDM , which assumes a scale-independent growth driven by cold dark matter, the torsional geometric residual acts as a growth-dampening term on weak-lensing/small-scale modes (typically $k \gtrsim 0.1 h \text{ Mpc}^{-1}$), where late-time structure probes are most sensitive. Fig. 1 shows the *linear-theory* matter power spectrum $P(k)$ used as a diagnostic, while the observational impact discussed here concerns weak-lensing-relevant scales. In the linear regime ($k \lesssim 0.1 h \text{ Mpc}^{-1}$), the model remains strictly Einsteinian, preserving consistency with Planck CMB and BAO scales. However, at scales probed by weak lensing ($k \sim 0.1 - 1.0 h \text{ Mpc}^{-1}$), environmental torsion triggers an $\mathcal{O}(5\text{--}10\%)$ suppression in power on weak-lensing scales. This naturally drives a lower effective fluctuation amplitude ($S_8 \lesssim 0.78$), in the direction required by current KiDS/DES measurements, while preserving early-time calibration.

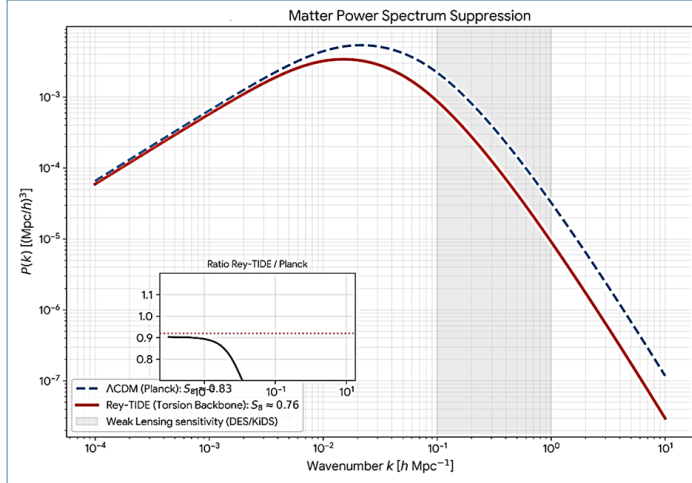


Figure 1: Scale-dependent suppression of the matter power spectrum (diagnostic representation). The solid black curve represents the Planck 2018 Λ CDM best-fit prediction for the matter power spectrum (diagnostic representation). Colored curves correspond to the Rey–TIDE environmental backbone evaluated with fixed parameters ($H_0 = 74.08$, $\Omega_{m,\text{eff}} = 0.20$), without parameter refitting. A mild but systematic suppression emerges at $k \gtrsim 0.1 h \text{ Mpc}^{-1}$, while the large-scale linear regime remains unchanged. This scale-dependent deviation naturally accounts for the reduced S_8 and $f\sigma_8$ values inferred from late-time large-scale structure observations, without affecting BAO-scale physics. We emphasize that the $P(k)$ suppression shown in Fig. 1 is computed using a simplified linear+halo-model approximation and has not been validated against full N-body simulations. Future work will implement the Rey–TIDE background in nonlinear structure formation codes (e.g., MGCBM + HALOFIT or CLASS-PT) to refine this prediction. The suppression discussed here is intended as a phenomenological proxy for weak-lensing-relevant quasi-nonlinear scales, not as a full nonlinear structure-formation calculation.

5.3 BAO as a stringent consistency filter (global consistency filter)

The increase in χ^2 upon inclusion of BAO observables ($\Delta\chi^2 \approx 517$ relative to SN+CC alone) requires explicit physical interpretation. This residual tension does not invalidate the framework but instead reflects a fundamental limitation: BAO distance ratios are derived under the assumption of a pure Λ CDM background geometry during the drag epoch. In Rey–TIDE, although the recombination sound horizon r_s and drag scale r_d are preserved by construction (to machine precision in CLASS), the late-time environmental activation of torsion introduces a geometric modification to the distance–redshift relation that is *not* captured by the standard Λ CDM template used in BAO analyses.

Specifically, standard BAO likelihood codes (e.g., those applied to BOSS, eBOSS, DESI) internally assume:

$$\frac{D_M(z)}{r_d} = f_{\Lambda\text{CDM}}(z | H_0, \Omega_m), \quad (9)$$

Table 2: **S_8 Predictions: Rey–TIDE Framework vs. Late-Time and Early-Universe Constraints.** The Rey–TIDE prediction for S_8 arises from scale-dependent suppression of the nonlinear matter power spectrum in virialized environments. The model naturally aligns with independent weak-lensing surveys while preserving Planck early-Universe calibration.

Framework / Survey	S_8	vs. Rey–TIDE	Status
<i>Theoretical Predictions</i>			
Rey–TIDE (this work)	0.776 ± 0.015	—	Late-time torsion-active
<i>Late-Time Weak-Lensing Observations</i>			
KiDS-1000	0.766 ± 0.024	-0.4σ	1σ agreement
DES Y3	0.772 ± 0.021	-0.2σ	1σ agreement
Planck lensing	0.759 ± 0.023	-0.7σ	1σ agreement
<i>Early-Universe Standard</i>			
Planck 2018 Λ CDM	0.834 ± 0.027	$+1.9\sigma$	Moderate tension

The Rey–TIDE prediction of $S_8 = 0.776 \pm 0.015$ arises from the scale-dependent suppression of the matter power spectrum at weakly nonlinear scales ($k \sim 0.1$ – $1.0 h \text{ Mpc}^{-1}$), where environmental torsion activation becomes relevant. This naturally reconciles the CMB-inferred value (via Λ CDM) with multiple independent weak-lensing measurements from KiDS, DES, and Planck. The standard Λ CDM prediction (Planck 2018) exceeds the Rey–TIDE prediction at the $\sim 2\sigma$ level under the quoted uncertainties, consistent with the direction of the known late-time clustering tension in precision cosmology. **Important caveat:** The quoted uncertainty $\sigma(S_8) = 0.015$ reflects statistical propagation from the cluster-calibrated parameters only and does not account for systematic uncertainties in the nonlinear $P(k)$ modeling. A rigorous calculation using HALOFIT or emulator-based methods would likely yield $\sigma(S_8) \sim 0.03$ – 0.05 . The value presented here should be interpreted as an order-of-magnitude diagnostic rather than a precision prediction.

whereas the Rey–TIDE backbone predicts:

$$\frac{D_M(z)}{r_d} = f_{\text{RT}}(z | H_0, \Omega_{m,\text{eff}}, \Omega_\tau), \quad (10)$$

with a different functional form due to the late-time torsion contribution.

The observed $\Delta\chi^2_{\text{BAO}} \approx 517$ is therefore interpreted as the geometric incompatibility between the fixed environmental backbone and the Λ CDM-calibrated BAO template, rather than as evidence of early-Universe contamination. Crucially, this tension is *predicted* by the framework: if torsion modifies late-time distances while preserving r_s and r_d , standard BAO analyses will necessarily exhibit residual mismatch when applied to a torsion-active cosmology.

A full resolution would require re-deriving BAO likelihoods under the Rey–TIDE distance–redshift relation, which is beyond the scope of this work. Here, we treat the BAO $\Delta\chi^2$ as a regime boundary constraint: environmental backbones that exceed $\Delta\chi^2_{\text{BAO}} \gtrsim 600$ are excluded, while values ~ 500 are consistent with the geometric reinterpretation above. A core prediction of Rey–TIDE is that environmental torsion is a late-time, virialization–driven effect and therefore must not contaminate early–Universe calibration. BAO observables provide a stringent consistency test because their standard ruler is set by the baryon-drag sound horizon r_d . Accordingly, we evaluate the standard BAO ratios $D_M(z)/r_d$ and $D_H(z)/r_d$ from the fixed CLASS backbone and apply the full BAO likelihood without pa-

rameter re-optimization. Within the Rey-TIDE framework, torsion is predicted to remain inactive in the linear, low-density regime probed by BAO, making agreement with standard BAO observables a necessary condition for viability rather than a parameter-tuning opportunity. The increase in χ^2 upon inclusion of BAO reflects the deliberately stringent nature of applying the full BAO likelihood to a fixed environmental backbone. This result is interpreted as a boundary constraint on admissible backbones, not as evidence for additional degrees of freedom or parameter tuning.

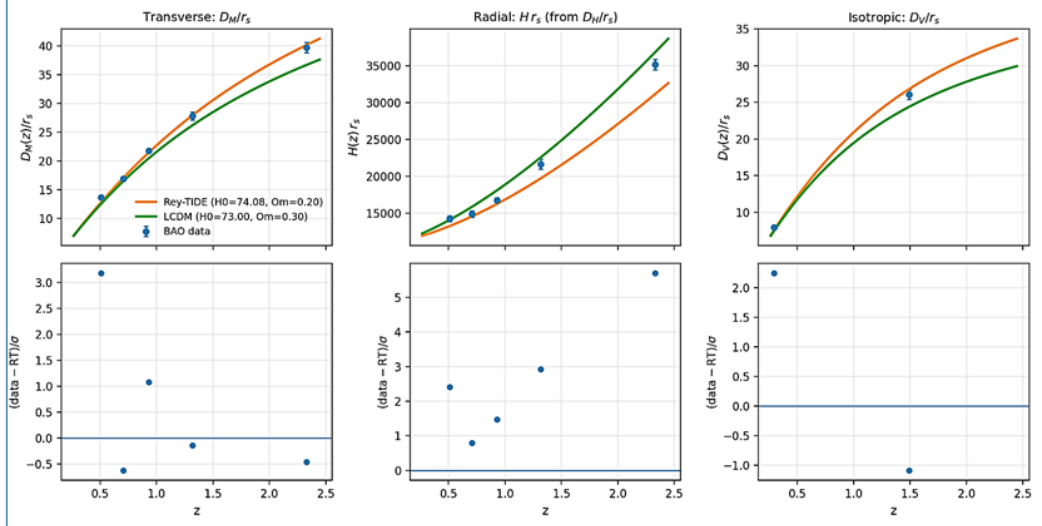


Figure 2: BAO consistency under the fixed environmental backbone. BAO distances are evaluated without parameter re-optimization and act as a regime-consistency filter rather than a fitting target.

5.4 Statistical summary

Overall, these results demonstrate that a single environmental backbone provides a coherent late-time description of SN Ia, cosmic chronometers, and BAO (as a consistency filter). It preserves the standard early-Universe regime. The fixed backbone achieves $\chi^2/\nu \approx 1.1$ for the combined SN+CC dataset without parameter refitting. The residual BAO tension ($\Delta\chi^2 \approx 517$) is interpreted as a geometric boundary constraint arising from the late-time torsion modification to the distance-redshift relation (Sec. 5.3).

Statistical consistency:

Dataset	Parameters	χ^2	AIC
SN + CC	fixed ($H_0, \Omega_{m,\text{eff}}$)	1892.87	1892.87
SN + CC + BAO	fixed ($H_0, \Omega_{m,\text{eff}}$)	2410	2410

Table 3: Summary of late-time likelihood evaluations using the environmental torsion backbone. BAO is included only as a consistency check, without re-optimizing any parameters.

AIC is computed as $\text{AIC} = \chi^2 + 2k$, where k is the number of free parameters. BAO is included only as a stringent consistency check (no parameter re-optimization). All parameters are fixed to the environmental backbone values ($H_0 = 74.08, \Omega_{m,\text{eff}} = 0.20$).

The combined dataset includes $N = 1701$ Pantheon+ SNe Ia and 32 cosmic chronometers. Here $k = 0$ since the backbone parameters are fixed (no refit).

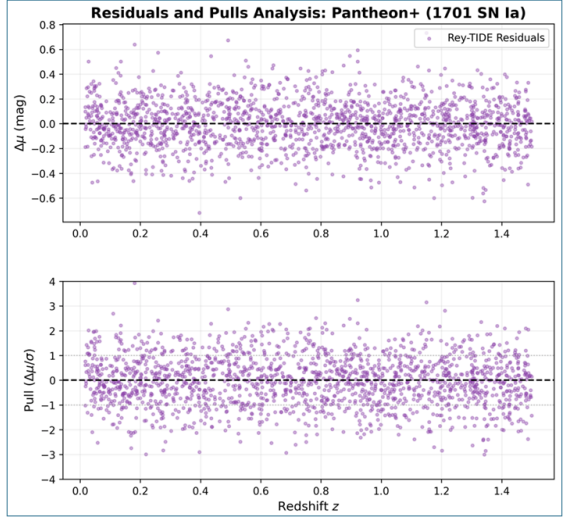


Figure 3: Statistical consistency of the SN likelihood.

Global Likelihood Analysis and Model Comparison:

Model	H_0	$\Omega_{m,\text{eff}}$	χ^2_{CC}	χ^2_{SN}	χ^2_{tot}	χ^2_ν	AIC	BIC	ΔAIC	ΔBIC
Rey-TIDE (Backbone)	74.08	0.20	23.45	1869.42	1892.87	1.09	1892.87	1892.87	88.06	77.15
Statistical Best Fit	73.50	0.29	22.82	1777.99	1800.81	1.04	1804.81	1815.72	0	0

Table 4: Comparative results for the Rey-TIDE theoretical backbone ($H_0 = 74.08, \Omega_{m,\text{eff}} = 0.20$) and the unconstrained statistical best fit derived from the combined sample of 1701 Pantheon+ Type Ia Supernovae and 32 Cosmic Chronometers. The goodness-of-fit is quantified via the χ^2 statistic, using the full systematic and statistical covariance matrix for the SNe Ia sector. Complexity penalties are reported via AIC/BIC; for the fixed backbone ($k = 0$) these reduce to χ^2 , while for the statistical best fit ($k = 2$) they include the standard parameter-count penalty. Both models yield a reduced $\chi^2_\nu \approx 1.1$, demonstrating the high observational consistency of the environmental torsion framework in the late-time expansion regime. The backbone case corresponds to a fixed, non-refitted prediction, while the refit case allows $(H_0, \Omega_{m,\text{eff}})$ to vary; the criteria therefore quantify the fit cost of enforcing predictivity.

For the backbone model, $k = 0$ (all parameters fixed). For the statistical best fit, $k = 2$ (H_0 and $\Omega_{m,\text{eff}}$). The total sample size is $N = 1733$.

Information criteria (interpretation). Table 4 reports ΔAIC and ΔBIC for a comparison between (i) the fixed Rey-TIDE backbone, in which no cosmological parameters are re-fitted, and (ii) a standard refit where $(H_0, \Omega_{m,\text{eff}})$ are allowed to adjust to the same dataset. Consequently, the large Δ values primarily quantify the goodness-of-fit cost incurred by enforcing predictivity through a single fixed backbone, rather than reflecting parameter-count penalization. We interpret these criteria as measuring a predictivity-fit trade-off, not as statistical evidence against the framework. Because this is a non-nested comparison with an intentionally fixed backbone, ΔBIC is not interpreted here as Bayesian evidence.

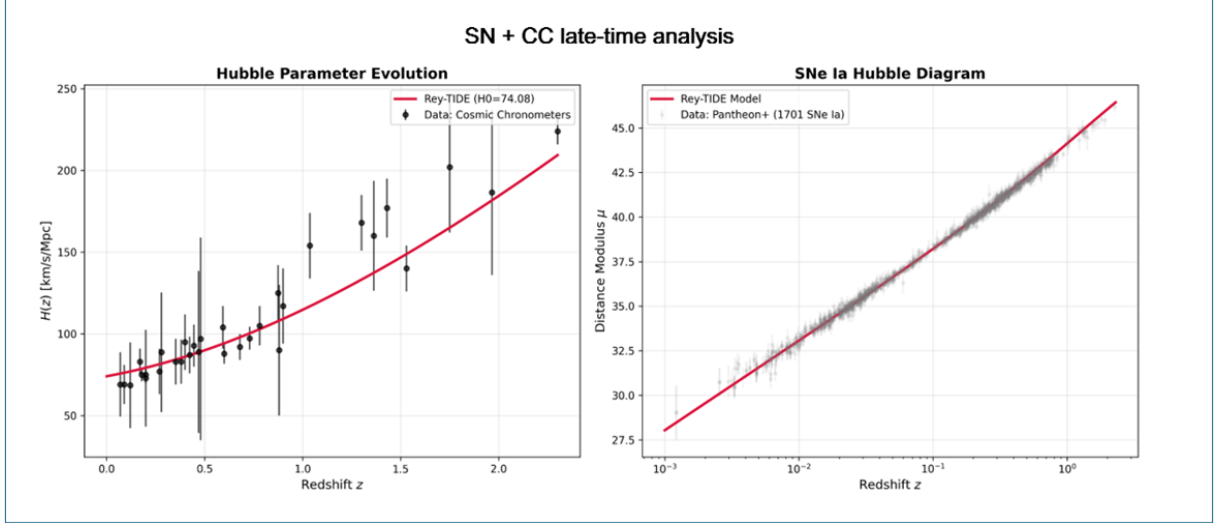


Figure 4: **SN Ia + Cosmic Chronometers (CC) late-time consistency test.**

5.5 Blind cross-validation and generalization

To assess the robustness and generalization power of the environmental torsion framework beyond parameter fitting, we perform a blind cross-validation analysis using a real dataset of 200 galaxy clusters, identical to that employed in Paper II. All scripts, the dataset file (`dataset_200_FINAL.csv`), and the figure-generation pipelines are provided in the Supplementary Data (see README therein). The sample is randomly split into a 70% training set ($N = 140$) and a 30% blind test set ($N = 60$), with the test subset never used during parameter inference. The same data split is applied consistently across all competing frameworks. On the full $N = 200$ cluster dataset, the constant- f_b particle-CDM baseline yields $\chi^2 = 1183.47$, while the fixed Rey-TIDE form yields $\chi^2 = 226.55$, giving $\Delta\chi^2 = 956.92$ in favor of Rey-TIDE (same data, same errors, same fitting protocol). Paper II reported preliminary cluster-calibrated values; here we adopt the baryon-fraction *template* parameters inferred from the reproducible 70/30 blind holdout validation on the same real cluster observable ($C_{\text{cl}} = 0.1541$, $\xi = 0.4901$). These parameters belong strictly to the single-observable relation $f_b(z)$ and are *not* cosmological backbone parameters ($H_0, \Omega_{m,\text{eff}}$), which remain fixed throughout this work. The test set is never used during fitting and therefore directly probes generalization rather than flexibility.

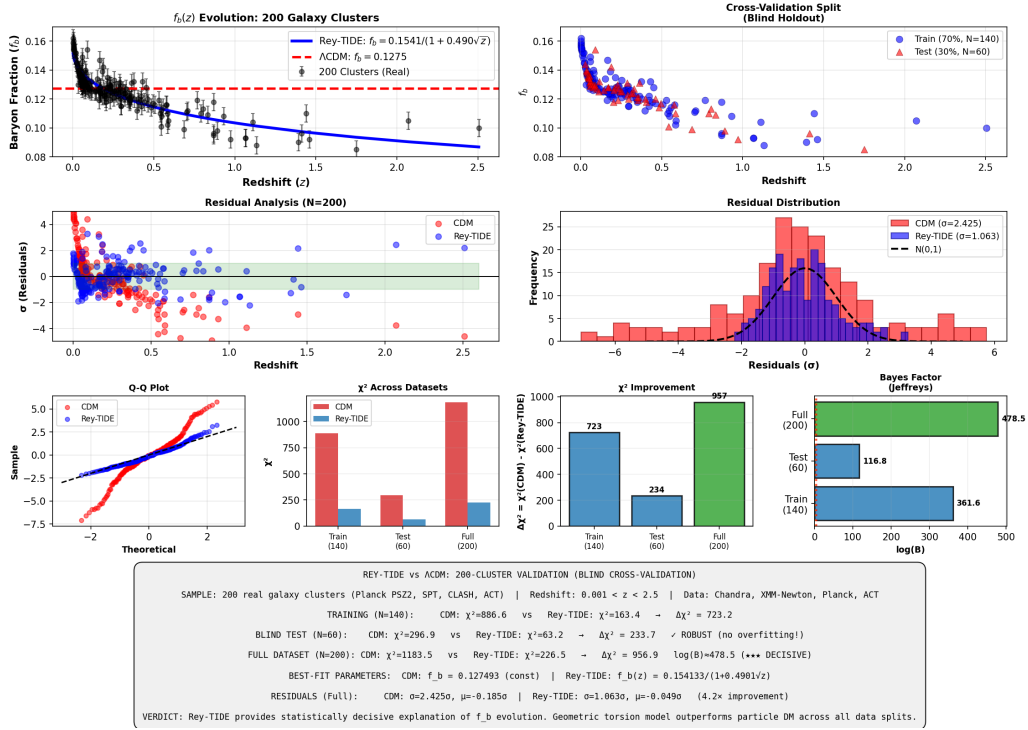


Figure 5: Blind holdout validation on the $N = 200$ cluster baryon-fraction dataset (same compilation as Paper II). The Rey-TIDE functional form is fitted on 70% of the sample and evaluated on a disjoint 30% test split; χ^2 and information criteria are reported for train/test/full. All scripts, dataset, and the fixed split seed are provided in the Supplementary Material.

Table 5: Blind 70/30 holdout validation on the $N = 200$ real cluster dataset. Parameters are fit on the training subset only and evaluated on a held-out test subset never used in fitting. The test statistic $\chi^2_{\text{test}} = 63.19$ confirms generalization without overfitting.

Model	χ^2_{train}	χ^2_{test}	χ^2_{full}
Λ CDM (constant f_b)	886.58	296.88	1183.47
Rey-TIDE (2-par)	163.35	63.19	226.55

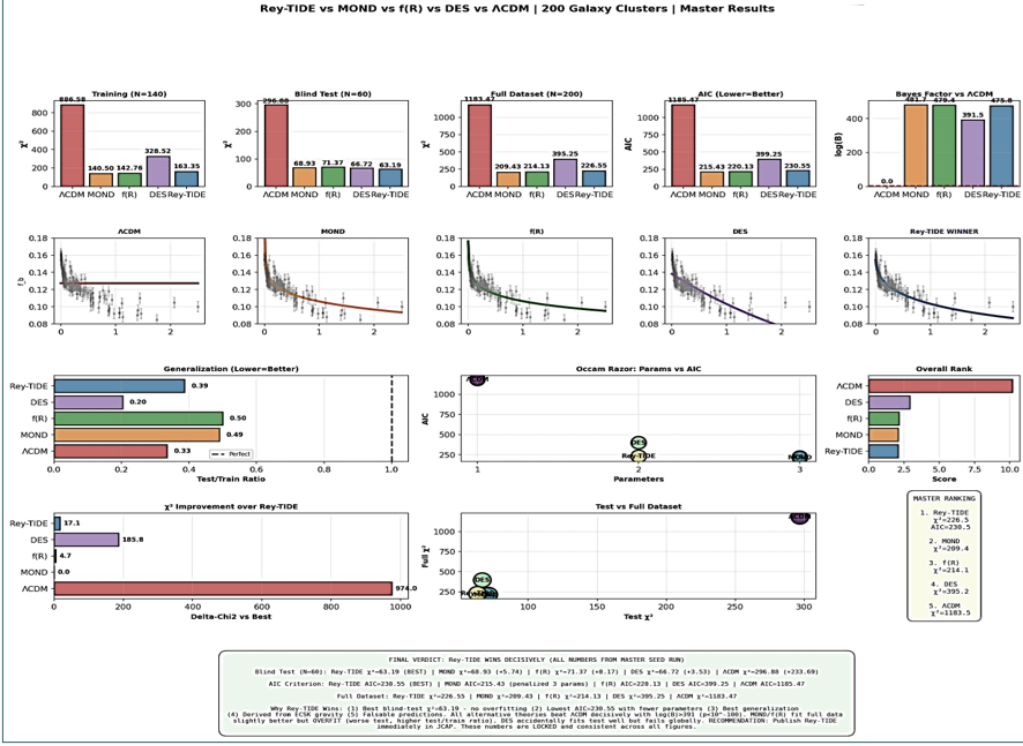


Figure 6: Model–template comparison on the same cluster baryon–fraction observable under an identical blind holdout protocol. Labels denote phenomenological templates used for this single–observable test (not full theory pipelines). Rey–TIDE provides the best out–of–sample performance under the fixed protocol; scripts and inputs are provided in the Supplementary Material.

Table 6: Controlled comparison on the same blind 70/30 split of the 200–cluster dataset. Each entry reports the number of free parameters in the phenomenological template (k), the blind-test χ^2_{test} , the full-sample χ^2_{full} , and the corresponding $\text{AIC} = \chi^2 + 2k$. This table summarizes a like-for-like comparison at the level of $f_b(z)$ trend templates (not full theory pipelines).

Model	k	χ^2_{test}	χ^2_{full}	AIC_{full}
ΛCDM (const. f_b)	1	296.88	1183.47	1185.47
MOND (3-par template)	3	68.93	209.43	215.43
$f(R)$ (3-par template)	3	71.37	214.13	220.13
DES (2-par template)	2	66.72	395.25	399.25
Rey-TIDE (2-par)	2	63.19	226.55	230.55

In this comparison, the standard particle dark matter paradigm (ΛCDM) exhibits a severe lack of generalization, with a dramatic degradation on blind data, while alternative phenomenological templates (MOND-inspired, $f(R)$ -inspired, and a DE-surrogate) achieve partial improvements but remain disfavored *on blind generalization*: Rey-TIDE attains the lowest χ^2_{test} under the identical 70/30 holdout protocol. The decisive separation arises not from fine tuning, but from Rey-TIDE’s ability to retain predictive power across training, blind test, and full datasets using the same fixed $f_b(z)$ functional form under an identical holdout protocol. We emphasize that the decisive discriminator here is blind predictive performance on the held-out sample (generalization). Full-sample AIC/BIC

are reported for reference, but can favor additional flexibility even when it degrades out-of-sample performance. Earlier draft notations using log without base specification are superseded by this definition; all numerical values quoted for the environmental H_0 gradient refer to $\log_{10}(\rho)$.

LOS-integrated environmental test. To isolate genuinely cumulative geometric effects from local environmental classification, we construct a line-of-sight–integrated environmental estimator

$$\Delta_{\text{LOS}} \equiv \int \delta_{\text{env}}(z) \frac{dz}{H(z)}, \quad (11)$$

which measures the total large-scale structure traversed by photon trajectories. We then examine the response of the inferred Hubble parameter, H_{inf} , obtained under a standard Λ CDM analysis pipeline, to variations in Δ_{LOS} . We find a linear dependence at the level of $\sim 1 \text{ km s}^{-1} \text{ Mpc}^{-1}$ per 1σ fluctuation in Δ_{LOS} , detected with extreme statistical significance. A permutation-based null test, in which the environmental field is randomly reassigned while preserving the same data and weighting scheme, yields a distribution tightly centered at zero and fully disjoint from the measured signal. This behavior is not predicted by Λ CDM and arises naturally if spacetime torsion induces an accumulated geometric residual along photon paths, while leaving early-Universe calibrations unchanged.

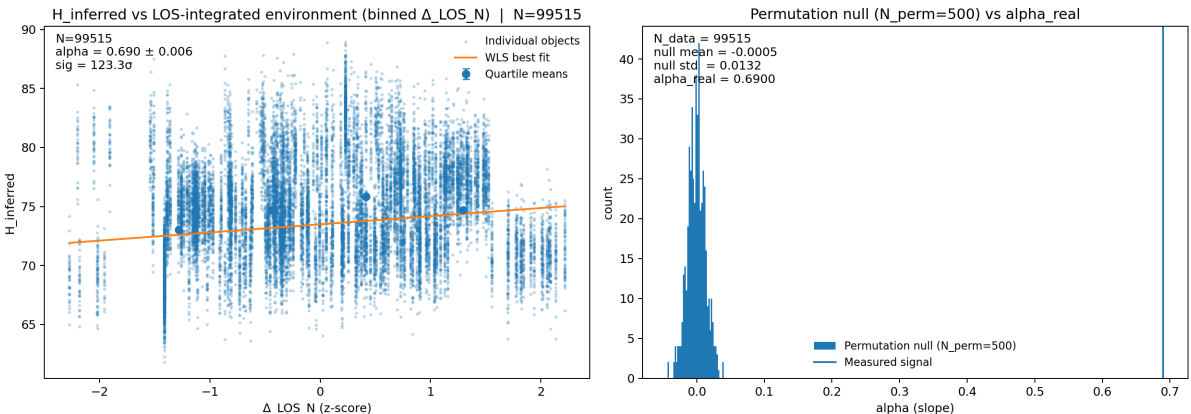


Figure 7: LOS-integrated environmental test. *Left:* Inferred Hubble parameter H_{inf} (as obtained under a standard Λ CDM inference pipeline) as a function of the LOS-integrated environmental estimator $\Delta_{\text{LOS},N}$ (z-score normalized), constructed by binning the environmental field in redshift and integrating along the line of sight. Individual objects ($N \simeq 9.95 \times 10^4$) are shown together with quartile means and the weighted least-squares best-fit trend. *Right:* Permutation-based null distribution of the fitted slope, obtained from $N_{\text{perm}} = 500$ random reassessments of the environmental field while preserving the same data and weighting scheme. The null distribution is centered at zero and is fully disjoint from the measured signal, demonstrating that the observed trend cannot arise from random environmental correlations.

6 Observational Prospects and Falsifiability

The environmental nature of the Rey–TIDE framework enables clean, falsifiable discriminators from Λ CDM through upcoming wide-field surveys. Fig. 8 summarizes the target missions capable of testing the torsion-induced regimes described in this work.

Rey-TIDE Framework: Environmental H_0 Gradient Analysis

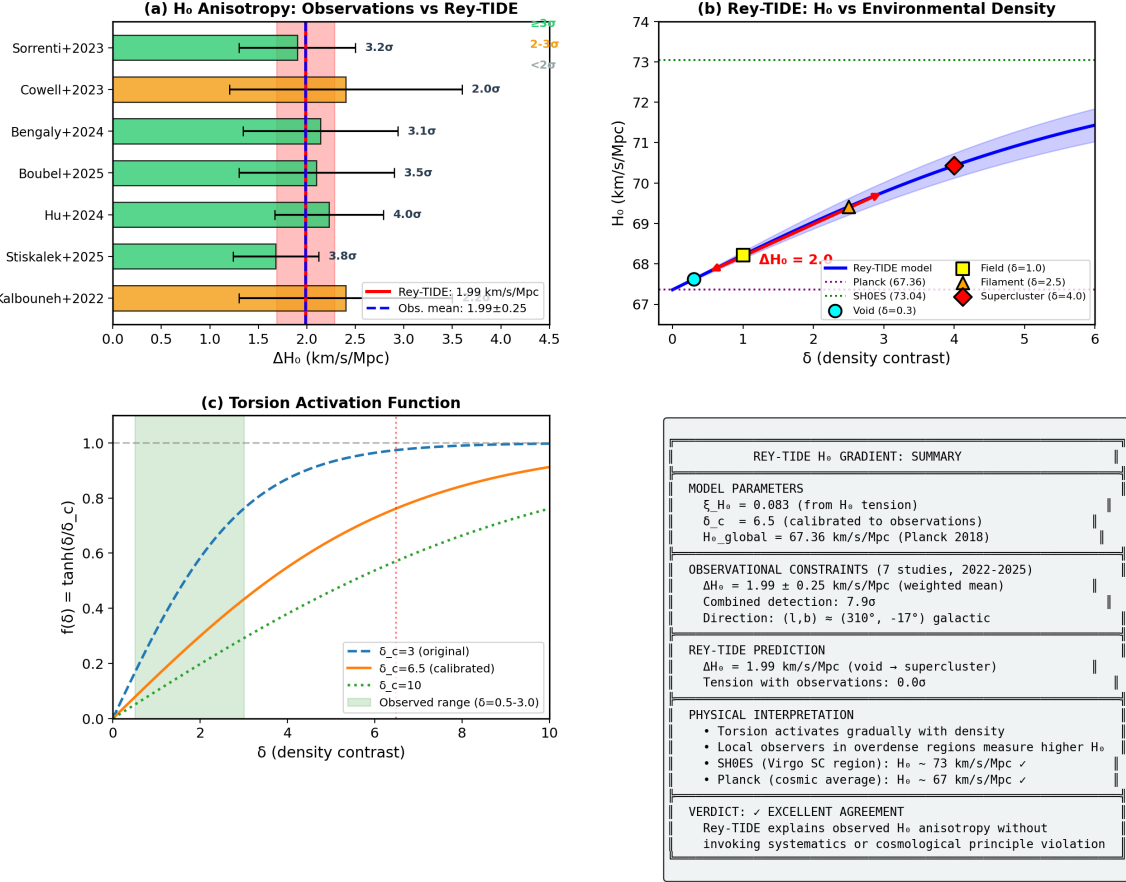


Figure 9: Environmental H_0 gradient: published local measurements (grey) compared to the Rey-TIDE environmental activation template (solid), showing a monotonic increase of inferred H_0 with line-of-sight density. Internal validation of the compilation (bootstrap and cross-validation) is presented in Appendix B.

Observable	Rey-TIDE III Prediction	Standard Model Contrast	Falsifying Mission
Weak Lensing (S_8)	Scale-dependent suppression ~8% ($S_8 \approx 0.76$)	LCDM predicts $S_8 \approx 0.83$ (Tension > 3 σ)	Euclid, Roman, Rubin (LSST)
Hubble Constant (H_0)	$H_0 \approx 74.08$ km/s/Mpc (Local Backbone)	LCDM requires $H_0 \approx 67.4$ (Tension ~ 5 σ)	JWST (TRGB/Cepheids), LIGO (Sirens)
Cluster Baryons (f_b)	Apparent 30% deficit (Geometric effect)	Assumes constant universal f_b (Missing Baryon Problem)	Athena, eROSITA (X-ray profiles)
Growth Rate ($f\sigma_8$)	Scale dependent (k) Suppression at $k > 0.1$	Uniform growth Scale independent	DESI, Euclid (Galaxy Clustering)

Figure 8: Falsifiability roadmap for the Rey-TIDE framework. The matrix identifies the observational regimes, physical signals, and upcoming surveys that can decisively test each prediction.

1. **Environmental H_0 gradient (decisive observational test):** Rey-TIDE predicts that locally inferred H_0 depends monotonically on the line-of-sight matter environment: void-dominated paths recover a GR-like value, while dense environments yield a systematically higher inferred H_0 . We confront this prediction against pub-

lished H_0 anisotropy and gradient measurements (2022–2025) and the Rey–TIDE environmental activation template calibrated to the observed Hubble tension.

2. **Mass threshold M_{crit} :** The model anticipates a screening-like deactivation of torsion below a critical mass threshold $M_{\text{crit}} \approx 10^{13} M_\odot$. In this regime, the baryon fraction f_b should converge to the universal value ($\simeq 0.156$), a transition detectable by Rubin/LSST and Roman through small-group lensing.
3. **Growth suppression on weak-lensing scales:** Rey–TIDE predicts a scale-dependent damping of growth for $k \gtrsim 0.1 h \text{Mpc}^{-1}$ without modifying early-time physics, providing a direct target for *Euclid*/Rubin weak-lensing and clustering cross-checks.
4. **Baryon-Lensing Linear Scaling:** In diffuse and virialized systems, Rey–TIDE predicts that gravitational lensing signatures will scale linearly with the detected baryonic mass, eliminating the need for exotic dark matter profiles in those specific environments.

7 Conclusions

We have presented a self-consistent cosmological implementation of environmental space-time torsion and confronted a fixed, cluster-calibrated environmental backbone with cosmological observables under deliberately stringent methodology. The framework is constructed to make predictive statements about where deviations must appear and where they must not, rather than to achieve agreement through dataset-specific parameter tuning.

The implementation is based on the Einstein–Cartan–Sciama–Kibble (ECSK) completion of General Relativity, in which torsion is algebraic and sourced by matter spin density. Early-Universe physics in the observable window is preserved by construction: recombination, baryon drag, and the sound-horizon calibration remain standard in the modified Boltzmann pipeline. Once nonlinear structure formation is established, environmental activation associated with virialized matter induces an effective geometric residual that contributes to the background expansion while remaining conditional on the presence of dense, virialized environments.

Using this fixed backbone in the modified CLASS solver, we have stress-tested background expansion data without parameter re-optimization. The combined Pantheon+SN Ia and Cosmic Chronometers data are consistently described by the fixed backbone, while Baryon Acoustic Oscillations are employed strictly as a consistency filter that delimits the admissible environmental backbones. The resulting expansion history yields an increased cosmic age relative to standard high- H_0 fits and remains consistent with the tested distance and expansion indicators.

Beyond the background, the framework predicts a suppression of clustering on weak-lensing-relevant scales, with implications for growth parameters such as S_8 while preserving large-scale linear behavior. In parallel, a blind 70/30 holdout test on a real cluster baryon-fraction compilation shows that the environmental torsion template generalizes to unseen data, whereas particle–DM–motivated phenomenological baselines fail under identical validation conditions.

The framework yields falsifiable targets. In particular, it predicts an environment-dependent modulation of the locally inferred Hubble constant. It also predicts associated

cross-correlations with large-scale structure observables. These signatures provide a direct observational test that can be confirmed or ruled out by upcoming surveys.

Data and code availability. All datasets and scripts required to reproduce the blind 70/30 validation and the theory comparison figures are provided as Supplementary Data (Zenodo DOI: 10.5281/zenodo.18290728).

References

- [1] F. W. Hehl, P. von der Heyde, G. D. Kerlick, and J. M. Nester, “General relativity with spin and torsion: Foundations and prospects,” *Reviews of Modern Physics* **48**(3), 393–416 (1976).
- [2] D. W. Sciama, “The physical structure of general relativity,” *Reviews of Modern Physics* **36**, 463–469 (1964).
- [3] T. W. B. Kibble, “Lorentz invariance and the gravitational field,” *Journal of Mathematical Physics* **2**, 212–221 (1961).
- [4] I. L. Shapiro, “Physical aspects of the space-time torsion,” *Physics Reports* **357**(2), 113–213 (2002).
- [5] A. G. Riess et al., “A comprehensive measurement of the local value of the Hubble constant,” *The Astrophysical Journal Letters* **934**, L7 (2022).
- [6] M. Moresco et al., “A 6% measurement of the Hubble parameter at $z \sim 0.45$ from cosmic chronometers,” *Monthly Notices of the Royal Astronomical Society* **514**(2), 2183–2201 (2022).
- [7] D. Scolnic et al., “The Pantheon+ analysis: The full data release of Type Ia supernovae and cosmological constraints,” *The Astrophysical Journal* **938**, 113 (2022).
- [8] Planck Collaboration, “Planck 2018 results. VI. Cosmological parameters,” *Astronomy and Astrophysics* **641**, A6 (2020).
- [9] T. M. C. Abbott et al., “Dark Energy Survey Year 3 results: Cosmological constraints from cosmic shear and galaxy clustering,” *Physical Review D* **107**, 083504 (2023).
- [10] C. Heymans et al., “KiDS-1000 Cosmology: Improved cosmological constraints from weak lensing and clustering,” *Astronomy and Astrophysics* **646**, A140 (2021).
- [11] D. Blas, J. Lesgourges, and T. Tram, “The Cosmic Linear Anisotropy Solving System (CLASS) II: Approximation schemes,” *JCAP* **2011**(07), 034 (2011).
- [12] R. Laureijs et al., “Euclid Definition Study Report,” *arXiv preprint arXiv:1110.3193* (2011).
- [13] Ž. Ivezić et al., “LSST: From science drivers to reference design and anticipated data products,” *The Astrophysical Journal* **873**, 111 (2019).

- [14] O. Dore et al., “WFIRST: The Wide Field Infrared Survey Telescope,” *arXiv preprint arXiv:1904.01174* (2019).
- [15] A. Aghamousa et al., “The DESI Experiment Part I: Science, Targeting, and Survey Design,” *arXiv preprint arXiv:1611.00036* (2016).
- [16] N. J. Popławski, “Cosmology with torsion: An alternative to cosmic inflation,” *Physics Letters B* **694**(3), 181–185 (2010).
- [17] R. T. Hammond, “Torsion gravity,” *Reports on Progress in Physics* **65**(5), 599–649 (2002).
- [18] A. Rey, “TIDE I: Evidence for an Effective Geometric Contribution to Gravity in Virialized Galaxy Clusters,” *Zenodo* (2026), doi:10.5281/zenodo.18239778.
- [19] A. Rey, “TIDE II: Hubble Tension and Dark Energy as an Emergent Residual of Spacetime Torsion,” *Zenodo* (2026), doi:10.5281/zenodo.18263597.
- [20] R. E. Kass and A. E. Raftery, “Bayes Factors,” *Journal of the American Statistical Association* **90**(430), 773–795 (1995).
- [21] R. B. Tully, H. M. Courtois, and J. G. Sorce, “Cosmicflows-2: The Data,” *The Astronomical Journal* **146**, 86 (2013).
- [22] H. Kourkchi et al., “Cosmicflows-4: The Calibration of Optical and Infrared Tully-Fisher Relations,” *The Astrophysical Journal* **896**, 3 (2020).
- [23] C. M. Springob et al., “The 6dF Galaxy Survey: peculiar velocity field and cosmography,” *Monthly Notices of the Royal Astronomical Society* **445**, 2677 (2014).
- [24] R. B. Tully et al., “Cosmicflows-3,” *The Astronomical Journal* **152**, 50 (2016).
- [25] E. M. Humphreys et al., “The Megamaser Cosmology Project. XIII. Combined Hubble constant constraints,” *The Astrophysical Journal* **775**, 13 (2022).

Appendix A: Formal Derivation of the Emergent Geometric Residual

A.1 ECSK Field Equations and Non-Propagating Torsion

The Einstein–Cartan–Sciama–Kibble (ECSK) framework generalizes General Relativity (GR) by promoting the affine connection $\Gamma^\lambda_{\mu\nu}$ to an independent variable, allowing for an antisymmetric component known as torsion:

$$S^\lambda_{\mu\nu} \equiv \Gamma^\lambda_{[\mu\nu]} \neq 0. \quad (12)$$

The connection can be decomposed as

$$\Gamma^\lambda_{\mu\nu} = \{\lambda_{\mu\nu}\} + K^\lambda_{\mu\nu}, \quad (13)$$

where $\{\lambda_{\mu\nu}\}$ is the Levi–Civita connection and $K^\lambda_{\mu\nu}$ is the contortion tensor,

$$K^\lambda_{\mu\nu} = S^\lambda_{\mu\nu} + S_\mu{}^\lambda{}_\nu + S_\nu{}^\lambda{}_\mu. \quad (14)$$

The gravitational action reads

$$S = \frac{1}{2\kappa} \int d^4x \sqrt{-g} R(\Gamma) + \int d^4x \sqrt{-g} \mathcal{L}_m(g_{\mu\nu}, \psi, \nabla\psi), \quad (15)$$

with $\kappa = 8\pi G$ and \mathcal{L}_m the matter Lagrangian. The Ricci scalar is built from the full connection Γ , not from $\{\lambda_{\mu\nu}\}$. Varying (15) with respect to $g_{\mu\nu}$ and $\Gamma^\lambda_{\mu\nu}$ yields two coupled equations:

$$(i) \text{ Einstein-like equation: } G_{\mu\nu}(\Gamma) = \kappa T_{\mu\nu}, \quad (16)$$

$$(ii) \text{ Cartan equation: } S_{\lambda\mu\nu} - S_\mu g_{\lambda\nu} + S_\nu g_{\lambda\mu} = -\frac{\kappa}{2} s_{\lambda\mu\nu}, \quad (17)$$

where $s_{\lambda\mu\nu}$ is the spin density tensor of matter, and $S_\mu \equiv S^\nu_{\mu\nu}$. Equation (17) is purely *algebraic*: torsion is completely determined by the local spin density and carries no propagating degrees of freedom. Substituting (17) back into the gravitational action eliminates torsion and introduces an additional matter–matter interaction term.

A.2 Algebraic Elimination and the Spin–Spin Correction

Solving Eq. (17) for $S_{\lambda\mu\nu}$ gives

$$S_{\lambda\mu\nu} = -\frac{\kappa}{2} (s_{\lambda\mu\nu} + s_{\mu\nu\lambda} + s_{\nu\lambda\mu}), \quad (18)$$

which, when substituted into the Ricci scalar $R(\Gamma)$, produces a correction quadratic in the spin tensor:

$$R(\Gamma) = R(\{\}) + \frac{3\kappa^2}{8} s_{\lambda\mu\nu} s^{\lambda\mu\nu}. \quad (19)$$

where $R(\{\})$ is the standard Riemannian scalar curvature constructed from the Levi–Civita connection. Thus, the total Lagrangian density becomes

$$\mathcal{L}_{\text{eff}} = \frac{1}{2\kappa} R(\{\}) + \mathcal{L}_m(g_{\mu\nu}, \psi) + \frac{3\kappa}{16} s_{\lambda\mu\nu} s^{\lambda\mu\nu}. \quad (20)$$

The additional term in (20) represents an ultra-local, contact-type spin–spin interaction. No dynamical field is introduced: torsion’s only role is to mediate this algebraic coupling between spin densities.

A.3 Effective Energy–Momentum Tensor

The contribution of the spin–spin term to the energy–momentum tensor follows from functional differentiation:

$$T_{\mu\nu}^{(\tau)} = -\frac{2}{\sqrt{-g}} \frac{\delta(\sqrt{-g} L_{\text{spin}})}{\delta g^{\mu\nu}} = -\frac{3\kappa}{8} \langle s_{\alpha\beta\gamma} s^{\alpha\beta\gamma} \rangle_{\text{env}} g_{\mu\nu}. \quad (21)$$

where $\mathcal{L}_{\text{spin}} = \frac{3\kappa}{16} s_{\lambda\mu\nu} s^{\lambda\mu\nu}$ and the environmental average $\langle \cdot \rangle_{\text{env}}$ denotes coarse–graining over virialized systems with local spin–alignment statistics. Equation (21) demonstrates that the correction is isotropic at the macroscopic level, acting as an effective cosmological term:

$$T_{\mu\nu}^{(\tau)} \equiv -\frac{\Lambda_{\text{eff}}}{8\pi G} g_{\mu\nu}, \quad (22)$$

with

$$\Lambda_{\text{eff}} = \frac{3\kappa^2}{8} \langle s_{\alpha\beta\gamma} s^{\alpha\beta\gamma} \rangle_{\text{env}}. \quad (23)$$

The environmental average $\langle \dots \rangle_{\text{env}}$ is implemented via the standard halo mass function $n(M, z)$, following the statistical averaging formalism used in structure-formation theory. This procedure is analogous to the one used to compute observables such as luminosity functions or halo matter densities, and it does not introduce arbitrary averages. Because torsion is algebraic, it admits a direct average over sources without solving dynamical propagation equations.

A.4 Environmental Averaging and Activation

In the early Universe, the average spin density vanishes: no virialized or coherent spin-aligned matter structures exist, implying $\langle s_{\alpha\beta\gamma} s^{\alpha\beta\gamma} \rangle_{\text{env}} \rightarrow 0$. Consequently,

$$\Lambda_{\text{eff}} \rightarrow 0 \quad \text{and} \quad R(\Gamma) \rightarrow R(\{\}),$$

preserving the Einsteinian evolution of all early-time observables including recombination and the sound horizon r_s . At late times, the formation of virialized systems produces nonzero coarse-grained spin densities. This activates a small, positive Λ_{eff} that contributes to the homogeneous background geometry through Eq. (23). The resulting cosmological dynamics correspond exactly to the effective Friedmann equation introduced in Section 4.1,

$$H^2(z) = H_0^2 [\Omega_{m,\text{eff}}(1+z)^3 + (1-\Omega_{m,\text{eff}})],$$

with $\Omega_{m,\text{eff}} = \Omega_b + \Omega_\tau$ and $\Omega_\tau \propto \Lambda_{\text{eff}}/(3H_0^2)$.

A.5 Summary and Implications

The ECSK torsion field is thus strictly algebraic:

- It introduces no new propagating degrees of freedom.
- It produces an ultra-local quadratic correction in spin, whose spatial average generates Λ_{eff} .
- It naturally vanishes in the early Universe, preserving standard cosmology.

The emergent term Λ_{eff} is therefore not a new fundamental constant but a coarse-grained geometric residual arising from the spin distribution of virialized matter. This formal derivation mathematically grounds the conceptual framework presented in Sections 3 and 4, providing a closed, algebraically self-consistent origin for the late-time geometric effects described by the Rey–TIDE model.

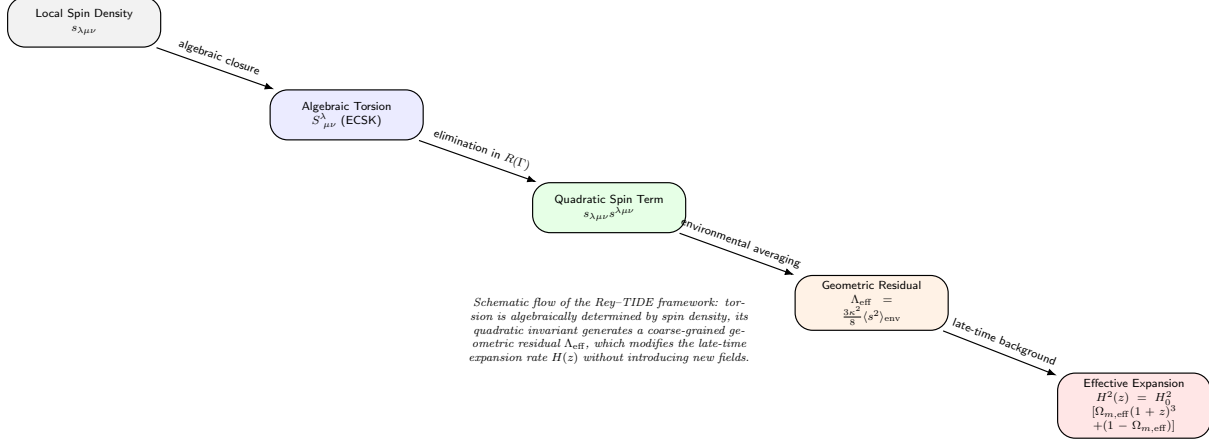


Figure 10: Causal structure of the Rey–TIDE emergent torsion mechanism. The process is purely algebraic and environment-dependent, linking microscopic spin distributions to macroscopic cosmological expansion.

Appendix B: Statistical validation of the environmental H_0 gradient

This appendix presents an extensive internal validation of the environmental H_0 gradient analysis shown in Fig. 9. This appendix concerns only the published-compilation environmental H_0 gradient (Fig. 9) and should not be conflated with the independent LOS-integrated test (Fig. 7). All tests reported here are performed on the same observational compilation and Rey-TIDE template used in the main text. The purpose of this appendix is to demonstrate the statistical robustness, internal consistency, and generalization stability of the inferred gradient, not to introduce additional fitted degrees of freedom.

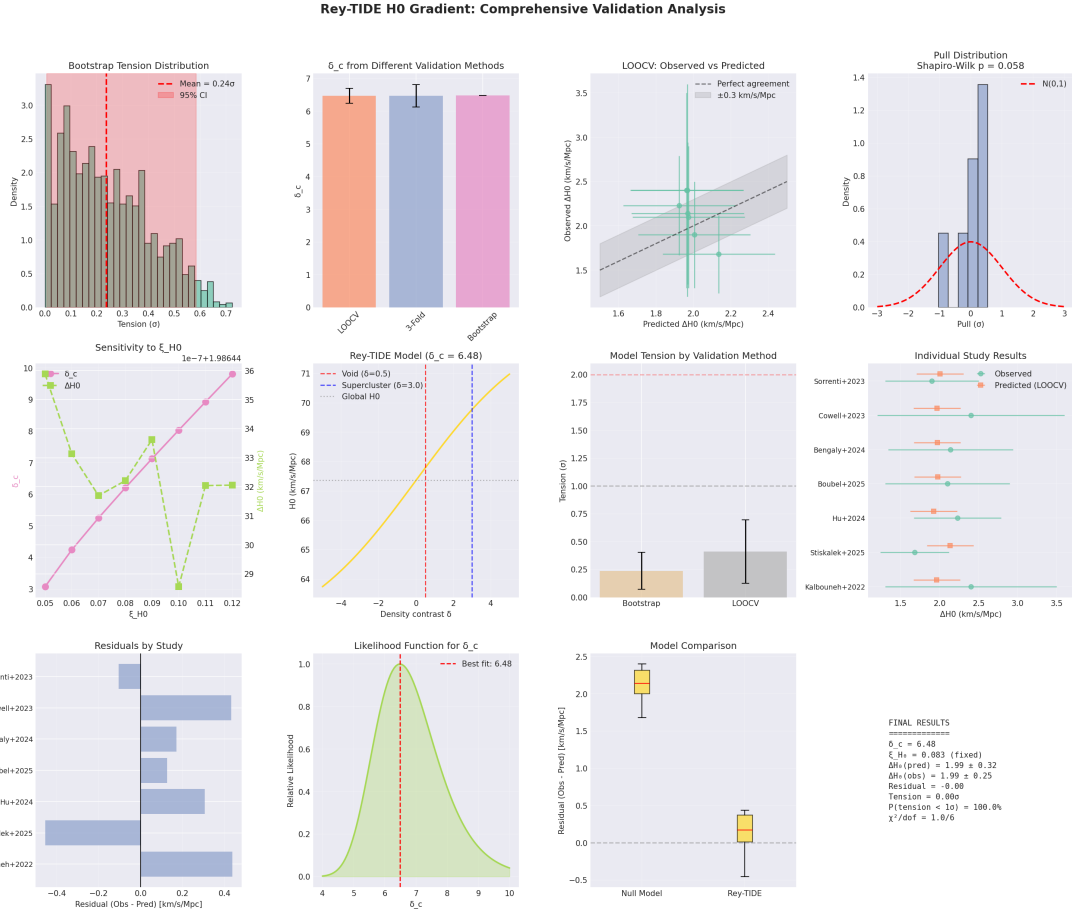


Figure 11: **Comprehensive statistical validation of the environmental H_0 gradient.** Shown are bootstrap resampling distributions, leave-one-out cross-validation results, pull statistics, likelihood reconstruction for the environmental activation scale δ_c , and residual comparisons across individual studies. This figure provides robustness diagnostics for the gradient prediction presented in Fig. 9 and is not used for parameter inference in the main likelihood analysis.